




# Photocatalytic activities of hydrothermal synthesized copper zinc tin sulfide nanostructures

Jitendra P. Sawant<sup>1</sup>, Rekha Rajput<sup>2</sup>, Seema Patil<sup>3</sup>, Jungho Ryu<sup>3</sup>, Deepak Rajaram Patil<sup>3,\*</sup> , and Rohidas B. Kale<sup>2</sup>

<sup>1</sup>Department of Physics, University of Mumbai, Santacruz (E), Mumbai 400098, India

<sup>2</sup>Department of Physics, The Institute of Science, Madam Cama Road, Mumbai 400032, India

<sup>3</sup>School of Materials Science and Engineering, Yeungnam University, Gyeongsan 38541, South Korea

Received: 14 May 2021

Accepted: 3 August 2021

Published online:

11 August 2021

© The Author(s), under exclusive licence to Springer Science+Business Media, LLC, part of Springer Nature 2021

## ABSTRACT

We report the hydrothermal synthesis of visible light absorbing and direct energy bandgap kesterite-structured  $\text{Cu}_2\text{ZnSnS}_4$  (CZTS) nanoparticles (NP) for photocatalytic and photoelectrochemical (PEC) applications. The crystal structure, morphology, composition, and optical properties of CZTS nanoparticles were analyzed using X-ray diffraction (XRD), scanning electron microscopy (SEM), and UV–Vis microscopy techniques. The tetragonal kesterite phase CZTS nanoparticles with compact spherical morphology with an energy bandgap of about 1.51 eV have been synthesized. The CZTS nanoparticles were employed as a photocatalyst for the degradation of Rhodamine B (RhB) dye. The study reveals that the CZTS photocatalysts with compact spherical shape showed photoactivity around 55% under indoor visible light illumination. The CZTS photoelectrodes were fabricated on fluorine-doped tin oxide (FTO) substrate using a doctor blade coating method. The detailed photoelectrochemical (PEC) studies demonstrate that CZTS photoelectrode showed 2.98% of photoconversion efficiency.

## 1 Introduction

Dyes are an important class of synthetic colored organic compounds that are used in many industries [1]. Consequently, they have become common industrial environmental pollutants during their synthesis and dyeing process. Therefore, it is essential to investigate an appropriate and environmentally friendly treatment for the disposal of these dyes. A number of biological and chemical treatments have

been increasingly explored and developed to treat the wastewater. Among the current pollution control technology biodegradation of dye by various microbes is emerged as an effective and promising approach [2]. However, the adsorption of dyes occurs only on the surface of the biosorbent, without undergoing degradation [3]. Some of the biological treatments such as aerobic and anaerobic processes are also not effective for certain dyes [4]. Physical methods like ion exchange, adsorption, and filtration

Address correspondence to E-mail: [deepphy24@gmail.com](mailto:deepphy24@gmail.com)

are also not effective because they simply transfer the dyes to another phase rather than degrading them [5]. Photocatalysis is an advanced oxidation process (AOP) in which photocatalyst accelerates the photo-generated electrons when interact with the light, offers a solution to those limitations. The AOP methods are relatively high efficient, cost-effective, and a green approach for the complete mineralization of hazardous pollutants [6].

Several photocatalysts have been tested for the degradation of organic pollutants.  $\text{TiO}_2$  and  $\text{ZnO}$  are excellent photocatalysts for the photocatalytic degradation of organic pollutants. However, the main drawback of these materials is the absorption region which is limited only to the ultraviolet region. Therefore, for the effective utilization of the solar spectrum, there is a need to develop semiconductor materials with bandgap in the visible range. The copper zinc tin sulfide (CZTS) has attracted intense attention because of its significant advantages such as less toxicity, low cost, and earth-abundant constituent elements [7]. The CZTS exists in two phases, which are kesterite and stannite with space group  $\Gamma 4$  and  $\Gamma 42m$  [8], respectively. These phases belong to tetragonal structures, with a cubic closely packed array of sulfur as an anion and cations located at one-half of the tetragonal void, with a stacking similar to zinc blend structure with lattice parameters  $a = 5.46 \text{ \AA}$  and  $c = 10.93 \text{ \AA}$  [8]. Especially, kesterite phase CZTS is a p-type semiconductor material that shows an excellent optical absorption about  $10^4 \text{ cm}^{-1}$  and a direct bandgap ( $E_g$ ) of about 1.45–1.7 eV [9–12], which makes this material well suited for the applications such as solar cells photocatalysis [11] and the gas sensors [13]. The kesterite phase CZTS shows excellent theoretical photoconversion efficiency as high as 32.2% [14].

Various physical and chemical methods have been reported to deposit CZTS thin films which include sputtering [15], thermal evaporation [16, 17], electrodeposition [18], and spray pyrolysis [19, 20]. The solution-based methods are the most successful approach to synthesize CZTS nanoparticles [21, 22]. However, due to several issues such as toxicity and environmentally harmful reaction solvent (oleylamine, hydrazine), these methods have limitations for the scalable manufacturing processes. Therefore, a green, reliable and non-toxic solvent-based solution process for CZTS synthesis is always favorable for its large-scale production [23, 24].

Herein, low cost and environmentally friendly hydrothermal route was used to synthesize the CZTS nanoparticles using water as a solvent. Some of the researchers have indeed used hydrothermal method for the synthesis of CZTS nanoparticles [25–32]. However, most of these studies were focused on the photovoltaic applications [25–32]. Therefore, in the present study we have synthesized CZTS nanoparticles using hydrothermal method and the films were fabricated on the FTO substrate using doctor blade technique. The structural, optical, and morphological properties of CZTS nanoparticles were investigated. Further, the performance of CZTS photoelectrode was analyzed using PEC measurements under indoor visible light irradiation.

## 2 Experimental section

### 2.1 Chemicals and materials

Cupric sulfate pentahydrate ( $\text{CuSO}_4 \cdot 5\text{H}_2\text{O}$ ), zinc sulfate ( $\text{ZnSO}_4 \cdot 7\text{H}_2\text{O}$ ), stannous chloride ( $\text{SnCl}_2 \cdot 2\text{H}_2\text{O}$ ), thiourea  $\text{CS} \cdot (\text{NH}_2)_2$ , ethylcellulose, terpineol, ethanol, fluorine-doped tin oxide substrate (FTO), and sodium sulfate ( $\text{Na}_2\text{SO}_4$ ) were purchased from S.D. Chem. Ltd., which were used without further purification.

### 2.2 Hydrothermal synthesis of CZTS nanoparticles

For the synthesis of CZTS nanoparticles, 0.01 M copper sulfate, 0.005 M zinc sulfate, 0.005 M tin chloride, and 0.08 M thiourea were dissolved in water. The resultant solution was stirred for 30 min and then transferred into a Teflon-lined stainless steel autoclave filled up to 75% of its capacity. The autoclave was kept in a hot air oven maintained at  $180 \text{ }^\circ\text{C}$  for 24 h. After that, the oven is kept for cooling naturally to room temperature. The precipitate was collected, washed with distilled water and ethanol several times, and dried in air at  $200 \text{ }^\circ\text{C}$  for 2 h [23, 24].

### 2.3 Fabrication of CTS/FTO photoelectrode

The CZTS thin films were deposited on the fluorine-doped tin oxide ( $\text{SnO}_2\text{:F}$ ) (FTO) glass substrate using the doctor blade coating method. The FTO substrate

was ultrasonically cleaned with distilled water. Initially, 10 mg of CZTS sample and 3 mg of ethyl cellulose were mixed and crushed together. A premixed solution of ethanol and terpineol (10:1) was added dropwise in the mixture containing CZTS and ethyl cellulose to form suitable viscous CZTS paste. The resulting paste was coated on the ultrasonic cleaned FTO substrate and annealed at 250 °C for 30 min. The CZTS/FTO electrodes were used as a photoelectrode to study the performance of the PEC cell. The schematics of the formation mechanism of CZTS nanoparticles using the hydrothermal process and the doctor blade coating method are depicted in Fig. 1.

### 2.4 Characterization techniques

X-ray diffraction (XRD) pattern was recorded using X-ray diffractometer (XPERT-PRO MPD), with  $\text{CuK}\alpha$  radiations of wavelength 1.5404 Å in  $2\theta$  range between 20° and 70°. The Raman spectrum of the sample was recorded using a Raman spectrometer in the range 600 to 2100  $\text{cm}^{-1}$ . The He-Ne laser with wavelength of 532 nm was used as an excitation source. The chemical composition and the morphology of CZTS nanoparticles were characterized by different characterization techniques such as energy-dispersive X-ray spectroscopy (EDS), scanning electron microscopy (SEM, JEOL JSM-IT300), transmission electron microscopy (TEM), selected area electron diffraction (SAED, CM20FEG, 200 kV), and high electron transmission microscopy (HRTEM,

JEOL JEM-2100F, 200 kV). The surface area and pore diameter of CZTS nanoparticles were calculated by the Brunauer–Emmett–Teller (BET) equation. The optical properties of the material were studied by UV–Vis (PerkinElmer) absorbance spectrophotometer at room temperature.

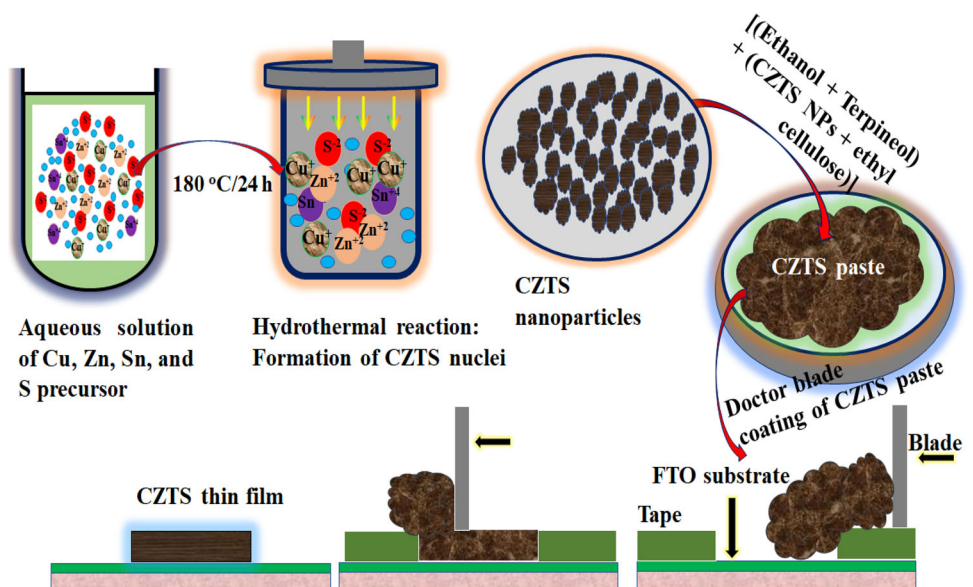
### 2.5 Photocatalytic activity measurement

The photocatalytic reaction was carried in a 750 ml glass cylindrical photochemical reactor. In a typical process, 10 mg of CZTS nanoparticles were mixed in 50 ml of 10 ppm aqueous solution of RhB dye. The solution was kept in dark for 24 h to achieve equilibrium. To study visible light degradation, the sample was illuminated with a 125 W mercury lamp and changes in concentration of dye were measured using UV–Vis absorption spectra at regular intervals of time. The absorption peak observed at 554 nm was used to determine the degradation of the RhB dye. The photodegradation efficiency of CZTS nanoparticles was calculated using the following formula [33]:

$$\text{Degradation efficiency(\%)} = \frac{A_0 - A_t}{A_0} \times 100 \quad (1)$$

where  $A_0$  is the initial absorbance of dye solution before the addition of a catalyst and  $A_t$  is the absorbance at time  $t$  after the addition of the catalyst. The reaction rate constant ' $k$ ' was determined using the following equation assuming the first order reaction kinetics:

**Fig. 1** Schematics of hydrothermal synthesis of CZTS nanoparticles and doctor blade coating of CZTS thin films



$$\ln \left[ \frac{A_t}{A_0} \right] = -kt \quad (2)$$

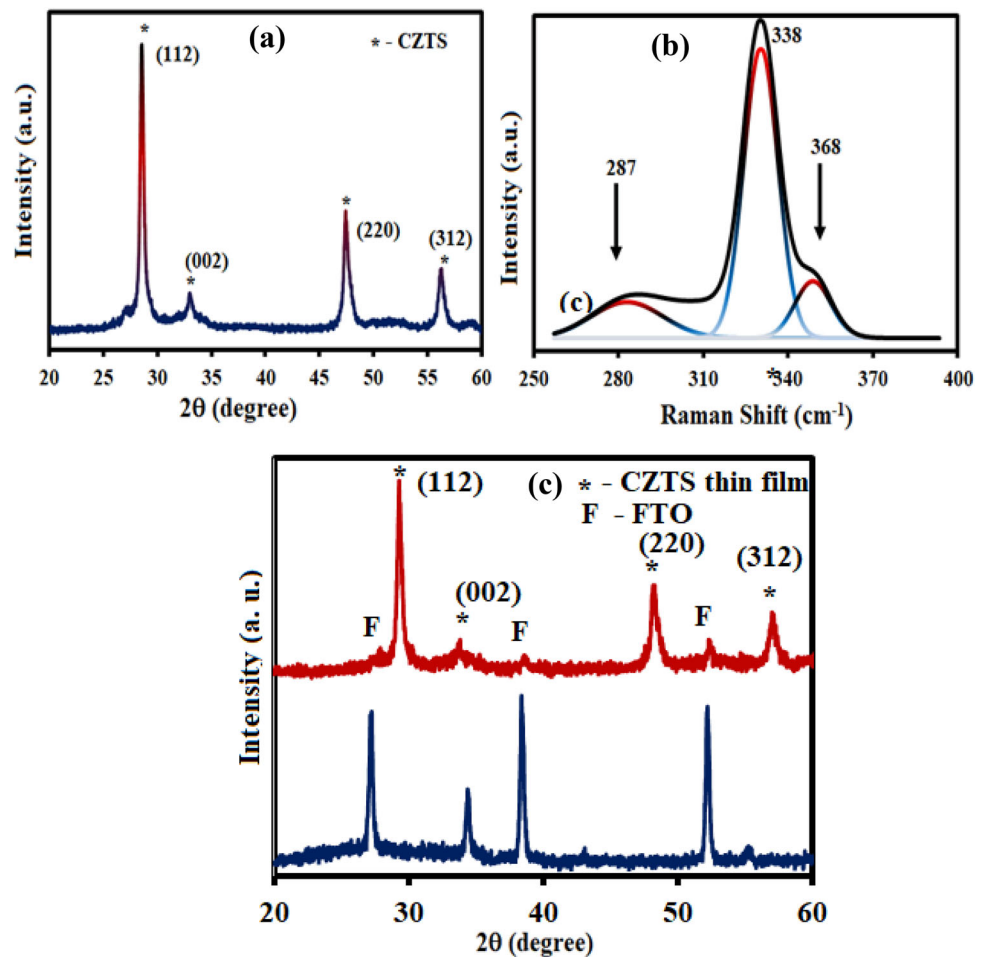
### 3 Results and discussion

#### 3.1 Structural analysis

Figure 2a depicts the XRD pattern of CZTS nanoparticles synthesized using the hydrothermal method and air annealed at 200 °C for 2 h. All the observed diffraction patterns match with the JCPDS-26-0575 reference of the tetragonal kesterite phase of CZTS [26]. The diffraction peak observed at  $2\theta = 28.45^\circ$ ,  $33.31^\circ$ ,  $47.79^\circ$  and  $56.21^\circ$  could be assigned to (112), (200), (220), and (312) planes of kesterite phase of CZTS, respectively. The lattice parameters calculated for CZTS nanoparticle considering (112) XRD peak are found to be  $a = 5.391 \text{ \AA}$  and  $c = 10.798 \text{ \AA}$ . The crystallite size estimated from

the Scherrer formula is found to be  $\sim 15 \text{ nm}$ . From the XRD pattern, it is seen that the intensity of the (112) peak is dominant in all the CZTS samples. It is to be noted that, there are no impurity peaks observed in the XRD pattern. The XRD pattern of some binary and ternary phase compounds is [34, 35] similar to that of CZTS. Therefore, to identify the kesterite phase CZTS compound, the only XRD pattern is not sufficient. Therefore, to confirm the phase purity, the Raman spectrum CZTS sample was recorded. The Raman spectrum showed three major peaks at positions  $287$ ,  $338$ , and  $368 \text{ cm}^{-1}$  as depicted in Fig. 2b. The XRD pattern of CZTS thin film deposited on FTO substrate is shown in Fig. 2c. These observations are in good agreement with reported values for kesterite phase CZTS [36, 37].

**Fig. 2** a XRD pattern of CZTS nanoparticles, b Raman spectrum of CZTS nanoparticles, c XRD pattern of CZTS thin film deposited on FTO substrate



### 3.2 Compositional and morphological studies

In order to estimate the elemental composition, the energy-dispersive spectroscopy (EDS) technique was employed. In the synthesis process, the ideal stoichiometric composition of  $\text{Cu}/(\text{Zn} + \text{Sn}) = 1$  and that of  $\text{Zn}/\text{Sn} = 1$  [36] of metal precursors was chosen. The EDS analysis showed a slight change in the composition of CZTS nanoparticles. The observed composition ratio of  $\text{Cu}/(\text{Zn} + \text{Sn})$  was 0.86 and  $\text{Zn}/\text{Sn}$  ratio was 0.918. For high-performance CZTS-based solar cell, the optimum composition ratio of  $\text{Cu}/(\text{Zn} + \text{Sn})$  and  $\text{Zn}/\text{Sn}$  was reported to be about 0.75 ~ 0.95 and 1.1 ~ 1.4, respectively [36, 37].

Figure 3a–d shows the SEM image of CZTS nanoparticles synthesized using the hydrothermal method. From the SEM images, it is seen that the grown CZTS nanoparticles exhibit coagulation of nanospheres. The morphology of CZTS nanoparticles was further investigated by HRTEM analysis. Figure 4a shows HRTEM images of the CZTS nanoparticles that reveal the relatively small particles

of ~ 15 nm size. Figure 4b shows the lattice fringe pattern of crystalline CZTS nanoparticles. The interplanar spacing corresponding to (112) peak is observed to be 0.318 nm, which is identical to the theoretical value of 0.31 nm. The SAED pattern shown in Fig. 4c indicates the polycrystalline nature of CZTS nanoparticles. The particle size distribution of CZTS nanoparticles from HRTEM images is depicted in Fig. 4d. The average particle size is 16.89 nm. The result of the HRTEM image indicates that the (112) plane is the preferred growth plane of CZTS nanoparticles.

### 3.3 Optical studies

The room temperature optical absorbance was recorded in the wavelength range of about 350–1100 nm. The bandgap energy was estimated by plotting the graph of  $(\alpha h\nu)^2$  versus  $(h\nu)$  and extra plotting with the energy axis as shown in Fig. 5. The direct bandgap of spherical CZTS nanoparticles was estimated to be 1.52 eV which is in good agreement with earlier reported values [23, 24, 38, 39].

**Fig. 3** SEM images of CZTS nanoparticles synthesized using the hydrothermal method at different magnifications

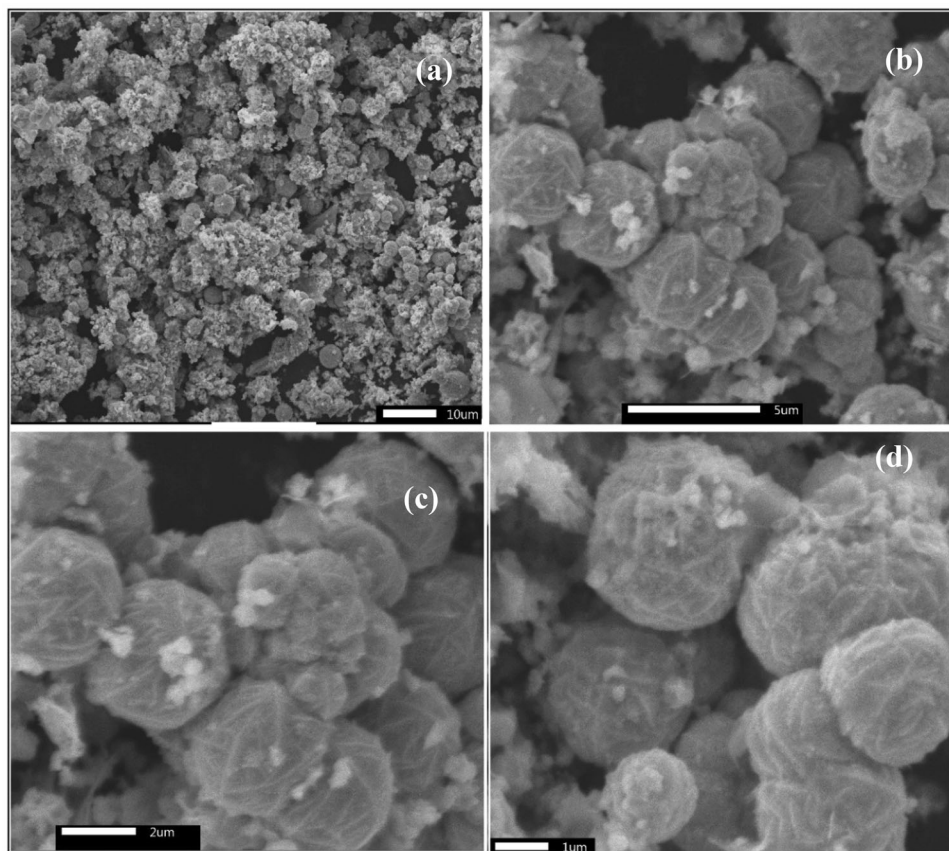
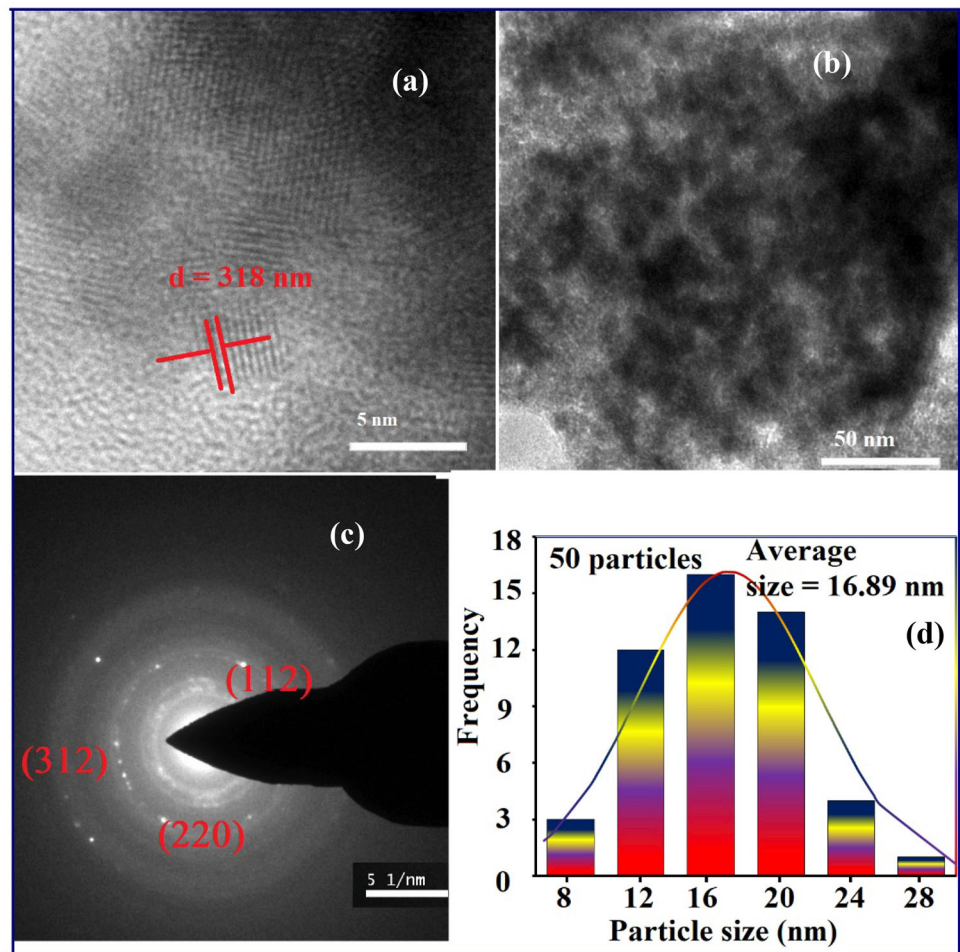


**Fig. 4** **a** HRTEM image of CZTS nanoparticles, **b** lattice fringe pattern showing d-spacing, **c** SAED pattern of CZTS nanoparticles, and **d** size distribution of CZTS nanoparticles in the CZTS sample

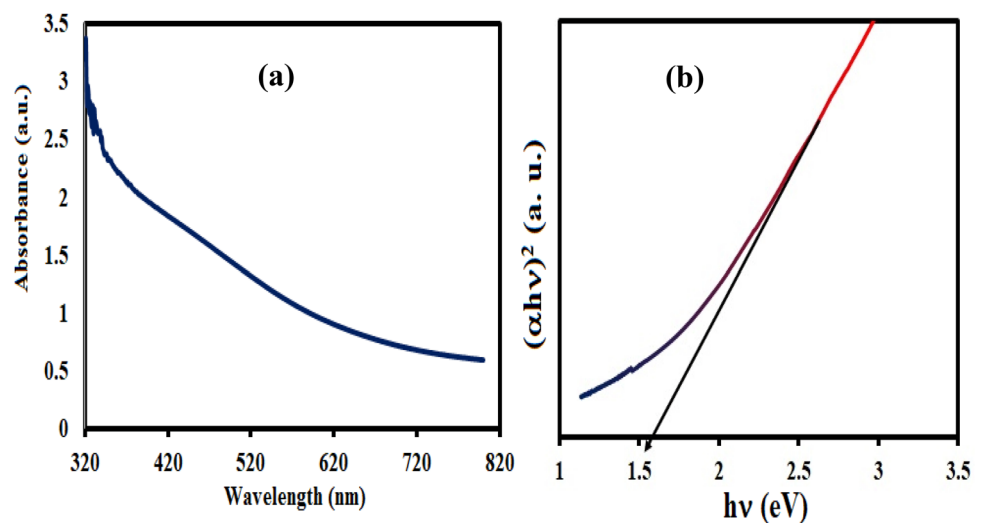


### 3.4 BET analysis

The CZTS nanoparticles were further analyzed by measuring  $N_2$  adsorption–desorption isotherm to

elucidate the surface area and pore volume. Figure 6 depicts the isotherm of CZTS nanoparticles displaying a hysteresis in the relative pressure range from 0.4 to 0.9. The surface area of CZTS nanoparticles

**Fig. 5** The plot of **a** absorbance vs wavelength of the CZTS thin film and **b**  $(\alpha hv)^2$  versus  $(hv)$  for estimation of bandgap energy of CZTS thin films



estimated using BET analysis was found to be 25.086 m<sup>2</sup>/g. The corresponding pore volume and pore size estimated were observed to be 0.029 cm<sup>3</sup>/g and 6.87 nm, respectively. The catalyst with a higher surface area showed enhanced catalytic activity [40, 41]. Also, the bandgap of photocatalyst should be compatible with the visible region, to improve the light absorption ability. The CZTS nanoparticles showed the highest surface area (25.086 m<sup>2</sup>/g) and showed a direct optical bandgap of around 1.52 eV. Therefore, CZTS nanoparticles are used to study the photocatalytic activity to degrade RhB dye.

### 3.5 Visible light-driven photocatalytic activity of CZTS nanoparticles

The CZTS nanoparticles were employed in the photocatalytic reactor and analyzed for degradation of RhB dye. The results indicating the variation of absorbance against the time of degradation of RhB dye in presence of CZTS nanoparticles are depicted in Fig. 7a. In the results, at around 554 nm, a gradual decrease in absorption intensity of RhB dye was observed over a given period [42]. A decrease in the absorption intensity indicates the degradation of RhB dye by CZTS under indoor light illumination. The percentage degradation efficiency of RhB dye was estimated using Eq. 1 and found to be 55% within 240 min. Yu et al. [43] reported 60%, 88%, and 95% degradation of RhB dye using silver and platinum-doped CZTS photocatalyst. The rate constant *k* was calculated using Eq. 2 and was found to be 0.0046 min<sup>-1</sup> as shown in Fig. 7c.

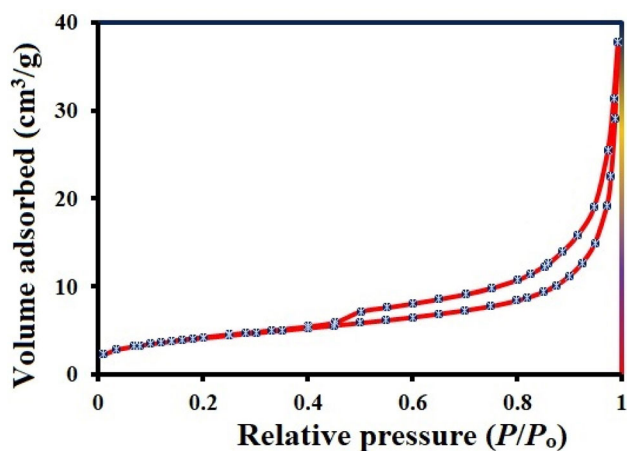
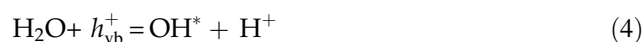
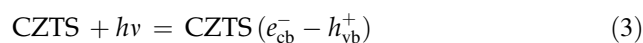


Fig. 6 The BET isotherm of CZTS nanoparticles

The CZTS nanoparticles absorb light photons of energy greater than the bandgap energy ( $E_g > h\nu$ ). The additional energy is transferred to the excited electrons and therefore electrons migrate from the valence band to the conduction band of CZTS, which results in the formation of electron–hole pairs (Eq. 3). The water molecules on the surface of CZTS nanoparticles get oxidized by positively charged holes and results in OH<sup>\*</sup> free radicals (Eq. 4). At the same time, the electrons from the conduction band are donated to molecular oxygen to form anionic superoxide radical O<sub>2</sub><sup>-\*</sup>, which further helps in the dissociation of water molecules and the formation of highly reactive OH<sup>\*</sup> hydroxyl radicals (Eqs. 5–7). The hydroxyl OH<sup>\*</sup> radicals generated are responsible for the photodegradation of RhB dye in an aqueous solution (Fig. 7d). The possible reaction mechanism of photodegradation is described in the following equations [44–46]:



The hydroxyl radicals OH<sup>\*</sup> are highly reactive, which would react with RhB dye to degrade it and produce non-toxic byproducts. The CZTS nanoparticles have been successfully used for photocatalytic degradation of methylene blue (MB), Rhodamine B (RhB), and trinitrotoluene (TNT) [46, 47]. Phaltane et al. reported 50% degradation of methylene blue (MB) by CZTS nanoparticle synthesized using the solvothermal method [48]. Apostolopoulou et al. studied the degradation of RhB dye using nanocrystalline CZTS thin films and reported 97.5% and 70% degradation of basic blue 41 (BB-41) and acidic orange 8 (AO-8) organic azo dye, respectively [49].

### 3.6 Photoelectrochemical (PEC) performance of CZTS thin films

The photoelectrochemical (PEC) properties were investigated using CH electrochemical analyzer instrument, with a three-electrode system consisting of CZTS as a photoelectrode, Pt as a counter

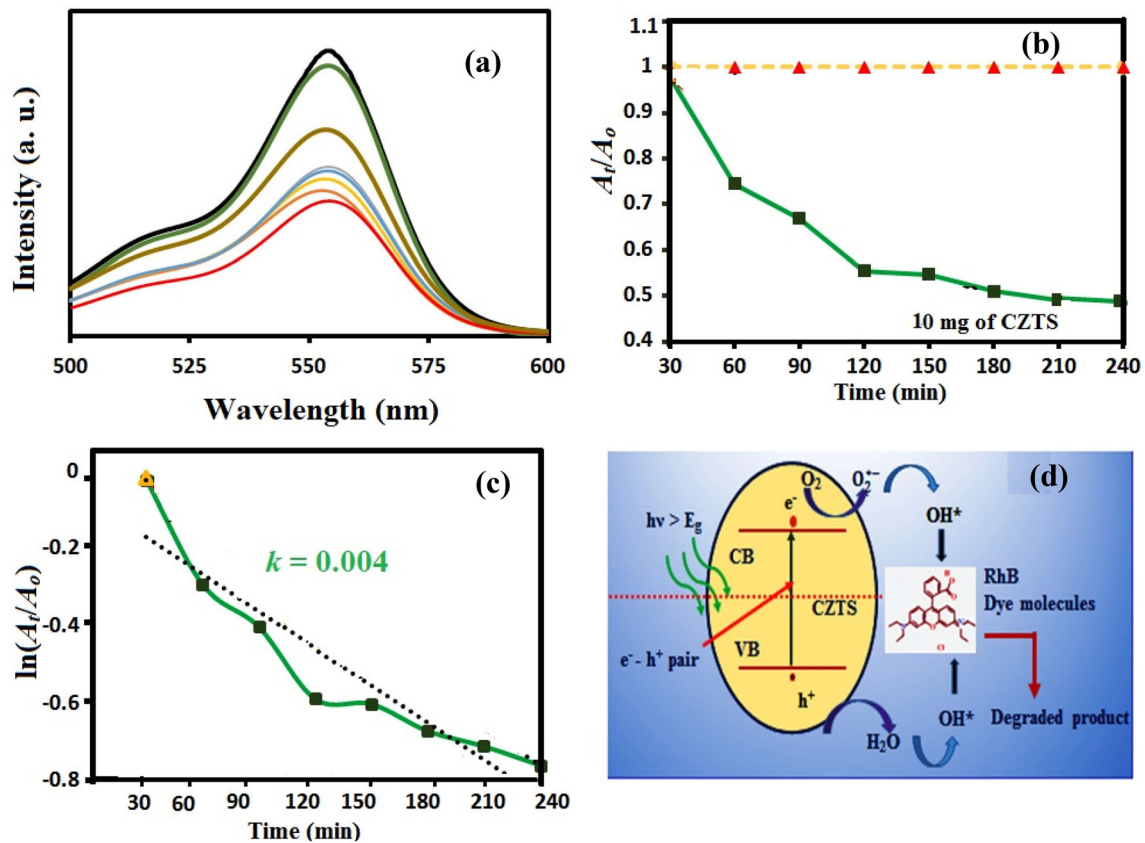


**Fig. 7** **a** Absorbance vs wavelength spectra of degradation of RhB dye by CZTS photocatalyst, **b** plot of  $A_t/A_0$  vs reaction time, **c** plot of the linear fit of  $\ln[A_t/A_0]$  vs reaction time for evaluation

electrode, and Ag/AgCl as a reference electrode. Three electrodes were immersed in the redox mediator containing 0.5 M aqueous solution of  $Na_2SO_4$  (pH = 6) solution under illumination. The sample was irradiated from the semiconductor electrolyte interface with a solar simulator with AM 1.5 G illumination ( $100 \text{ mW}/\text{cm}^2$ ). Various cell parameters like short-circuit current density ( $J_{sc}$ ), open circuit voltage ( $V_{oc}$ ), and photovoltaic conversion efficiency ( $\eta$ ) of the cell were estimated using the following equations:

$$FF = \frac{I_{max} V_{max}}{I_{sc} V_{sc}} \quad (10)$$

$$\eta(\%) = \frac{I_{sc} V_{ov}}{P_{in}} \times FF \times 100 \quad (11)$$

where FF is the fill factor,  $\eta$  is photoconversion efficiency,  $I_{max}$  is maximum current density,  $V_{max}$  is maximum voltage,  $J_{sc}$  is the short-circuit current density, and  $V_{oc}$  is the open circuit potential. The  $P_{in}$  is input power in  $\text{watt}/\text{cm}^2$ .

of a reaction rate constant of RhB dye degradation, **d** schematic illustration of photocatalytic activity by CZTS nanocrystals for the degradation of RhB dye under visible light

From the  $J$ - $V$  plot shown in Fig. 8, it is observed that the sample showed 2.98% of photoconversion efficiency with a current density ( $J_{sc}$ ) =  $8.87 \text{ mA}/\text{cm}^2$ , open circuit voltage ( $V_{ov}$ ) = 0.58 V, and fill factor (FF) = 58%. The composition of CZTS nanoparticles is slightly copper poor and zinc rich. The reduction in Cu concentration below the stoichiometric value results in the removal of Cu-based binary phases and leads to the optimized  $[Cu/(Zn + Sn)]$  composition ratio. The existence of the Cu vacancy ( $V_{Cu}$ ) and Cu-substituted Zn sites ( $Cu_{Zn}$ ) [42] at transition energies of 0.02 and 0.10 eV above the valence band maxima greatly influence the power conversion efficiency of the cell. The Cu poor composition of the film enhances the Cu vacancy ( $V_{Cu}$ ) formation and suppresses the copper-substituted Zn sites ( $Cu_{Zn}$ ), resulting in a higher short-circuit current density ( $J_{sc}$ ). The results showed that CZTS can be the significant candidate for application in solar cell devices [50, 51].



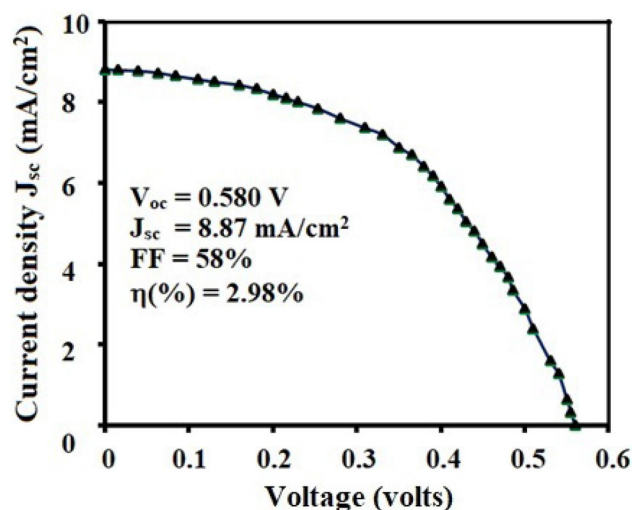


**Fig. 8** Current density ( $J_{sc}$ ) vs open circuit voltage ( $V_{oc}$ ) curve for CZTS photoelectrodes

#### 4 Conclusion

In this study, kesterite-structured CZTS nanoparticles were successfully synthesized by facile hydrothermal route. The analysis of XRD data showed formation of tetragonal kesterite phase of CZTS. The SEM images showed dense and compact coagulation of nanospheres. The HRTEM images showed the CZTS nanoparticles with the average size around  $\sim 15$  nm and (112) orientation is dominant. UV–Vis absorption spectra showed the direct bandgap-type CZTS with a bandgap energy of about 1.52 eV, which is optimum for the absorber layer of the solar energy. The CZTS nanoparticles were used as photocatalysts for the degradation of RhB dye. The CZTS nanoparticles as a photocatalyst displayed 55% degradation of RhB dye under visible light illumination for 4 h. The PEC device fabricated using CZTS photoelectrode has shown 2.98% of photoconversion efficiency. The results verify that the structural and optical properties make CZTS a potential candidate for photocatalyst as well as photovoltaic applications. Further research is underway to improve the photocatalytic and photovoltaic properties of CZTS compound semiconductors.

#### Acknowledgements

This research work is supported by the Department of Science and Technology, India under FIST (SR/FST/PSI-173/2012) program. The authors are

thankful to the Director, The Institute of Science, Fort, Mumbai, for the encouragement and providing the necessary facility. Authors are also thankful to INUP, as a part of the reported work (characterization) was carried out at IITBNF, and IITB under INUP which is sponsored by deity, MCIT, Government of India.

#### References

1. J.R. Aspland, *Textile dyeing and coloration*. (American Association of Textile Chemists and Colorists, Research Triangle Park, 1997), p. 354
2. Q. Husain, *Crit. Rev. Biotechnol.* **26**, 201 (2006)
3. M. Muruganandham, N. Sobana, M. Swaminathan, *J. Hazard. Mater.* **137**(3), 1371 (2006)
4. F. Han, V.S.R. Kambala, M. Srinivasan, D. Rajarathnam, R. Naidu, *Appl. Catal. A* **359**(1–2), 25 (2009)
5. N. Barka, S. Qourzal, A. Assabbane, Y. Ait-itchou, A. Nounah, H. Lachheb, A. Houas, *Arab. J. Sci. Eng.* **35**, 131 (2009)
6. T. Ali, Y.M. Hunge, A. Venkatraman, *J. Mater. Sci.: Mater. Electron.* **29**, 1209 (2018)
7. H. Zhou, W.C. Hsu, H.S. Duan, B. Bob, W. Yang, T.B. Song, C.J. Hsu, Y. Yang, *Energy Environ. Sci.* **6**, 2822 (2013)
8. S.R. Hall, J.T. Szymanski, J.M. Stewart, *Can. Mineral.* **16**, 131 (1978)
9. H. Katagity, *Thin Solid Films* **480**, 426 (2005)
10. A. Hiller, B. Miller, *Electrochem. Acta* **25**, 29 (1980)
11. C. Dun, W. Huang, H. Huang, J. Xu, N. Zhou, Y. Zheng, H. Tsai, W. Nie, D. Onken, Y. Li, D.L. Carroll, *J. Phy. Chem. C* **118**, 30302 (2014)
12. C. Shi, G. Shi, Z. Chen, P. Yang, M. Yao, *Mater. Lett.* **73**, 89 (2012)
13. S.J. Patil, R.N. Bulakhe, C.D. Lokhande, *J. Anal. Appl. Pyrolysis* **117**, 310 (2016)
14. S. Jung, J. Gwak, H.H. Yun, S. Ahn, D. Nam, H. Cheong, S. Ahn, A. Cho, K. Shin, K. Yoon, *Thin Solid Films* **535**, 52 (2013)
15. J. Seol, S. Lee, J. Lee, H. Nam, K. Kim, K. Sol, *Energy Mater. Sol. Cells* **75**, 155 (2003)
16. A. Weber, H. Krquth, S. Pertl, B. Schubert, I. Kotschau, S. Schorr, H. Schock, *Thin Solid Films* **517**, 2524 (2009)
17. K. Wang, O. Gunawan, T. Tordov, B. Shin, S.J. Chey, N.A. Bojarczuk, D. Mitzi, S. Guha, *Solar Cells* **97**, 143508 (2010)
18. C.P. Chan, H. Lam, C. Surya, *Energy Mater. Sol. Cells* **94**, 207 (2010)
19. N. Kamoun, H. Bouzouita, B. Rezig, *Thin Solid Films* **515**, 5949 (2007)
20. J.P. Sawant, H.M. Pathan, R.B. Kale, *ES Energy Environ.* (2020). <https://doi.org/10.30919/eseec8c933>

21. J. Kavalakkatt, X. Lin, K. Kornhuber, P. Kusch, A. Ennaoui, S. Reich, M.C. Lux-Steiner, *Thin Solid Films* **535**, 380 (2013)
22. M.T. Wang, O. Winkler, T. Gunawan, T.K. Gokmen, Y. Todorov, D.B. Zhu, D. Mitzi, *Adv. Energy Mater.* **4**, 1301465 (2014)
23. J.P. Sawant, R.B. Kale, *Mater. Lett.* **265**, 127407 (2020)
24. J.P. Sawant, R.B. Kale, *J Solid State Electrochem.* **24**, 461 (2020)
25. Q.B. Wei, P. Xu, X.P. Ren, F. Fu, *J. Alloys Compd.* **770**, 424 (2019)
26. S.M. Camara, L. Wang, X. Zhang, *Nanotechnology* **24**, 495401 (2013)
27. A.G. Kannana, T.E. Manjulavallia, J. Chandrasekaran, *Proced. Eng.* **141**, 15 (2016)
28. Y.M. Hunge, A.A. Yadav, S. Liu, V.L. Mathe, *Ultrason. Sonochem.* **56**, 284 (2019)
29. X. Hou, Y. Li, J.J. Yan, C.W. Wang, *Mater. Res. Bull.* **60**, 628 (2014)
30. S.A. Phaltane, S.A. Vanalakar, T.S. Bhat, P.S. Patil, S.D. Sartale, L.D. Kadam, *J. Mater. Sci.: Mater. Electron.* **28**, 11 (2017)
31. S.S. Shinde, *J. Semicond.* **36**, 073003 (2015)
32. J.M. Buriak, P.M. Kamat, K.S. Schanze, *ACS Appl. Mater. Interfaces* **6**, 118515 (2014)
33. Z. Zhou, P. Zhang, Y. Lin, E. Ashalley, H. Ji, J. Wu, H. Li, Z. Wang, *Nanoscale Res. Lett.* **9**, 477 (2014)
34. J. Kong, Z. Zhou, M. Li, W.H. Zhou, S.J. Yuan, R. Yao, Y. Zhao, S. Wu, *Nanoscale Res. Lett.* **8**, 464 (2013)
35. M. Li, W.H. Zhou, J. Guo, Y.L. Zhou, Z.L. Hou, J. Jiao, Z.J. Zhou, Z. Du, S. Wu, *J. Phys. Chem. C* **116**(50), 26507 (2012)
36. W.C. Jin, I. Agus, S.J. Park, W. Kim, S. Yoon, B.K. Min, *ACS Appl. Mater. Interfaces* **5**, 4162 (2013)
37. C. Zou, L.J. Zhang, D.S. Lin, Y. Yang, Q. Li, X.J. Xu, X. Chen, S.M. Huang, *CrystEngComm* **13**, 3310 (2011)
38. C. Persson, *J. Appl. Phys.* **107**, 053710 (2010)
39. Q. Tian, X. Xu, L. Han, M. Tang, R. Zou, Z. Chen, M. Yu, J. Yang, J. Hu, *CrystEngComm* **14**, 3847 (2014)
40. Y. Xia, B. Wang, X. Zhao, G. Wang, H. Wang, *Electrochim. Acta* **187**, 55 (2016)
41. G. Gogoi, S. Arora, N. Vinothkumar, M. De, M. Quereshi, *RSC Adv.* **5**, 40475 (2015)
42. M. Basu, A.K. Sinha, M. Pradhan, S. Sarkar, Y. Negishi, T. Govind, *Environ. Sci. Technol.* **44**, 6313 (2010)
43. X. Yu, A. Shavel, X. An, Z. Luo, M. Ibanez, A. Cabot, *J. Am. Chem. Soc.* **136**, 9236 (2014)
44. Z. Chen, D. Li, W. Zhang, Y. Shao, T. Chen, M. Sun, X. Fu, *J. Phys. Chem. C* **113**, 4433 (2009)
45. A. Houas, H. Lachheb, M. Ksibi, M. Elaloui, C. Guillard, J.M. Herrmann, *Appl. Catal. B* **31**, 145 (2001)
46. P. Kush, *Mater. Chem. Phys.* **162**, 608 (2015)
47. S.A. Phaltane, S.A. Wanalakar, T.S. Bhat, P.S. Patil, S.D. Sartale, L.D. Kadam, *J. Mater. Sci. Mater. Electron.* **28**, 8186 (2017)
48. A. Apostolopoulou, S. Mahajan, R. Sharma, E. Stathatos, *J. Phys. Chem. Solids.* **112**, 37 (2018)
49. S. Chen, J.H. Yang, X.G. Gong, A. Walsh, S.H. Wei, *Phys. Rev. B* **81**, 245204 (2010)
50. A.G. Kannan, T.E. Manjulavalli, J. Chandrasekaran, *Proced. Eng.* **141**, 15 (2016)
51. S.M. Camara, L. Wang, X. Zhang, *Nanotechnology* **24**(49), 495401 (2013)

**Publisher's Note** Springer Nature remains neutral with regard to jurisdictional claims in published maps and institutional affiliations.